Measurement 256 (2025) 118166

Contents lists available at ScienceDirect

Measurement

journal homepage: www.elsevier.com/locate/measurement

Fabrication and characterization of a piezo-MEMS uniaxial accelerometer as a tool for the monitoring of combustion instability in gas turbine engines

M.A. Signore [a,*], C. De Pascali [b], F. Quaranta [a], L. Velardi [a], D. Valerini [b], I. Farella [a], P. Di Gloria [c], M.G. De Giorgi [c], A. Ficarella [c], L. Francioso [a]

[a] CNR IMM, Institute for Microelectronics and Microsystems, Via Monteroni, I-73100 Lecce, Italy
[b] ENEA - Italian National Agency for New Technologies, Energy and Sustainable Economic Development, S.S. 7 Appia - km 706, 72100 Brindisi, Italy
[c] Department of Engineering for Innovation, University of Salento, Lecce, Italy

ARTICLE INFO

Keywords:
Piezoelectric accelerometer
Aluminum nitride
MEMS
Microfabrication
Combustion instability

ABSTRACT

This work is focused on the design, simulation, microfabrication, and characterization of an uniaxial piezoelectric MEMS accelerometer. It investigates the capability of the proposed device to monitor the combustion instability induced by the addition of air into jet-A1 fuel in a combustion chamber. The membrane structure of the accelerometer is modeled using the commercial FEM package COMSOL Multiphysics to optimize the geometrical parameters and validated through both analytical and experimental results. Aluminum nitride (AlN) thin film, deposited by sputtering process and characterized for its nanomechanical properties, was chosen as the active piezoelectric material of the accelerometer thanks to its compatibility with the complementary metal oxide semiconductor (CMOS) technology. The accelerometer has been characterized in terms of frequency response, sensitivity, and linearity. All experimental results, which are in good agreement with simulations, show that the functional characteristics of the accelerometer are as follows: resonance frequency of about 3.8 kHz; linear bandwidth in the range 0.3 – 1.2 kHz; dynamic sensitivity of 0.25 mV/g with a linearity of 99.1 %. Experiments for the monitoring of the combustion instability were conducted on a liquid-fueled swirling combustor with a nominal power of 300 kW at two global equivalence ratios (Φ), i.e. 0.36 and 0.18. The microfabricated accelerometer was positioned on the combustion chamber structure near the flame in the combustion zone for the measurement of the chamber vibrations. Its response was compared with the one of a commercial pressure sensor to assess its reliability, demonstrating good correlation between the signals coming from the two devices. Mean, variance and Kurtosis data analysis techniques were employed to elaborate signals coming from both sensors to provide a quantitative indicator of the combustion instability. Given its high sensitivity and wide linear bandwidth, the accelerometer can detect subtle variations in chamber vibrations, which are critical for early identification of combustion instability. By providing real-time, high-resolution monitoring, the device offers a non-invasive method for detecting and diagnosing instability phenomena that are often difficult to assess with traditional pressure sensors. The results demonstrate the potential of the realized piezoelectric accelerometer in understanding combustion instability mechanisms in gas turbines. Moreover, together with being a promising non-invasive tool of diagnosis of this phenomenon, the proposed solution is also expected to be a challenge for combustion instability prediction, contributing to the development of more stable combustors.

1. Introduction

Accelerometers are traditionally used for the measurement of mechanical parameters such as vibrations [1]. The monitoring and identification of abnormal vibrations during the working operations of mechanical components in aerospace, automotive, and industrial complex systems, are necessary to prevent damage and failure phenomena [2]. Among the different working mechanisms of accelerometers [3–6], piezoelectric one is the most accurate and reliable for vibration monitoring [7]. In addition, it allows for the mutual conversion between

* Corresponding author.
E-mail addresses: mariaassunta.signore@cnr.it (M.A. Signore), chiara.depascali@cnr.it (C. De Pascali), fabio.quaranta@cnr.it (F. Quaranta), luciano.velardi@cnr.it (L. Velardi), daniele.valerini@enea.it (D. Valerini), isabella.farella@cnr.it (I. Farella), pasquale.digloria@unisalento.it (P. Di Gloria), mariagrazia.degiorgi@unisalento.it (M.G. De Giorgi), antonio.ficarella@unisalento.it (A. Ficarella), lucanunzio.francioso@cnr.it (L. Francioso).

https://doi.org/10.1016/j.measurement.2025.118166
Received 24 February 2025; Received in revised form 11 June 2025; Accepted 12 June 2025
Available online 13 June 2025

vibration signals and electrical signals without the need for external power supply, promoting the development of no-power consumption devices [8]. Moreover, MEMS (Micro-Electro-Mechanical Systems) technology offers significant advantages over bulk technology including miniaturization, lightweight, low power requirement, cost-effectiveness, reliability, and simple integration into small scale systems. These benefits do not compromise the accelerometer's functionality, making MEMS-based piezoelectric accelerometers ideal for portable devices and compact systems [9]. Most commercially available piezoelectric accelerometers are based on bulky PZT (lead zirconate titanate), which exhibits excellent piezoelectric properties and high sensitivity [10], but it contains lead, a toxic element that poses environmental risks [11]. This has led to increased interest in lead-free materials such as ZnO and AlN, which offer promising performance without the environmental concerns associated with lead, though their lower piezoelectric coefficient results in slightly reduced sensitivity compared to PZT. As a lead-free material [12], AlN is compatible with MEMS fabrication processes, exhibits low dielectric losses, and can be easily deposited using reproducible methods, like sputtering [13]. It also offers a significantly higher maximum operating temperature compared to PZT, making it suitable for high-temperature applications. In recent years, accelerometers have been proposed as a practical tool for monitoring combustion instability, particularly in gas turbines [14]. Combustion instability, caused by the coupling of heat release fluctuations with the acoustic vibrations of the flame, results in high noise levels, abnormal vibrations, and potential structural damage [15]. Monitoring these vibrations is critical for early detection of instability and for mitigating the associated risks. The vibrations related to this phenomenon occur at discrete frequencies associated with the natural acoustic modes of the combustor, contrary to the case of combustion stability where the fluctuations are spanned in a very large bandwidth distributed in a wider frequency interval [16]. Specifically, the frequency bandwidth generally attributed to combustion-borne vibrations ranges from 0.3 to 1.5 kHz [17]. The increasing focus on monitoring combustion instability is driven not only by the need to improve engine performance but also by environmental concerns, because pollutants generated by combustion lead to acid rain, smog, and greenhouse gases [18]. The European Union has set a target to reduce greenhouse gas emissions by 40 % by 2030, making the development of efficient, stable combustion systems more critical than ever [19,20]. Accelerometers have been proposed as a possible alternative to overcome the known drawbacks of the conventional methods used by researchers to study combustion instability in laboratory-scale combustors [21,22], i.e. dynamic pressure sensors, Photo Multiplier Tube (PMT), high-speed imaging camera for chemiluminescence and OH– Planar Laser Induced Fluorescence (PLIF) [23,24]. In gas turbines, the most used commercial piezoelectric accelerometers are Endevco 6222 [25] and IMI sensor EX611A20 [26] which are macroscale devices.

This work proposes a MEMS-based uniaxial piezoelectric accelerometer for monitoring combustion instability in gas turbines by measuring the vibrations associated with this phenomenon. To the best of our knowledge, no existing literature has explored the use of MEMS-based piezoelectric accelerometers specifically microfabricated for combustion instability monitoring. The designed accelerometer consists of a circular proof mass suspended by a piezoelectric ring based on AlN thin film. The symmetry ensures the dominant movement along the axis perpendicular to the plane of the proof-mass, minimizing the contribution coming from the other two axes. The vibrations cause the oscillation of the suspended proof mass with the consequent deformation of the piezoelectric layer which generates electric charges. These charges are detected by a charge-to-voltage amplifier which output measures of the applied acceleration (vibration). The importance of the proposed work lies in the possibility of using microfabricated miniaturized piezo-MEMS accelerometer to monitor vibration signals coming from combustion chamber as a reliable non-invasive tool of diagnosis of combustion instability and damage prediction. The proposed accelerometer represents a significant advancement over the aforementioned traditional methods used to study combustion instability [22,23]. While these conventional methods provide valuable data, they often face challenges in real-world applications, including complex setup, bulkiness, and difficulty in integration into operational systems. In contrast, the proposed device provides a compact, reliable, and non-invasive solution for vibration measurement, which can be easily integrated into gas turbine systems. Our accelerometer not only ensures enhanced accuracy in monitoring combustion instability but also offers a practical alternative that overcomes many of the limitations inherent in the larger, more cumbersome equipment currently used.

In summary, the novelty of the work proposed can be highlighted in the following points:

- the design and development of a uniaxial piezoelectric MEMS accelerometer with a particular focus on the monitoring application for gas turbine combustion instability. To our knowledge, this is the first microfabrication process conceived to fulfill the special demands of this application.
- Application of AlN as the piezoelectric material, whose content is free from lead; it demonstrates even higher temperatures versus traditional PZT-based accelerometer devices that feature CMOS processes.
- The device herein presented assures a small-scale, precise, reliable measurement unit, compared with traditionally used measurement methodologies, namely the dynamic pressure sensors or high-speed cameras, that were in most situations unimplementable in a context of real factory production chains.
- By design, the accelerometer easily integrates into gas turbine systems and represents a practical means of monitoring combustion instability vibrations with less bulky equipment.
- The capability for combustion instability prediction and diagnosis could be realized with this accelerometer by monitoring the vibrations in real time, one of the main factors in the improvement of gas turbine engines for reliability and efficiency.

The paper is organized as follows: first, design, simulation and fabrication process of the piezoelectric accelerometer are presented. Then the results about the device characterization both in laboratory and in realistic working conditions are deeply discussed. Finally, in the conclusion section the main findings of the work are reported, highlighting the advantages of the proposed device compared to the traditional ones in the field of the combustion instability monitoring, and the future perspectives of its application.

2. Experimental details

2.1. Design and simulation of the piezoelectric accelerometer

The piezoelectric uniaxial accelerometer was designed using COMSOL Multiphysics. The 3D model comprises a circular membrane constituted by a 10 μm-thick Si device layer and a 1 μm-thick thermal SiO_2. The Si membrane is fully clamped to the edge and has a central circular proof mass of thickness 400 μm on the backside. The model was developed by using the *Solid Mechanics, Layered Shell, Electric Currents in Layered Shells*, and *Electric Circuit* physics interfaces, properly coupled with *Piezoelectricity* and *Layered Shell-Structure Transition*. The *Solid Mechanics* interface modeled the elastic behavior of the silicon membrane with an added proof mass. The piezoelectric ring is a multilayer placed in the high-strain annular region between the clamped edge and the proof mass. It comprises a 0.5 μm-thick AlN film sandwiched between two 0.2 μm-thick Ti electrodes. The piezoelectric ring was modeled by the layered shell technology, based on the layerwise theory [27]. The multilayer was defined using a surface (2D) geometry and a virtual extra dimension (1D) geometry in the through-thickness direction. Both the thickness and materials properties of each layer were

explicited, and the governing equations were solved within the spanned local 3D space. The *Layered Shell* and *Electric Currents in Layered Shells* interfaces enabled the accurate simulation of the coupled electromechanical behavior of the piezoelectric ring and its interaction with the surrounding mechanical structure. The piezoelectric coupling was formulated using the stress-charge form:

$$T = c_E S - e^T \boldsymbol{E}$$

$$\boldsymbol{D} = eS + \varepsilon_0 \varepsilon_r \boldsymbol{E}$$

where S denotes the strain tensor, c_E is the elasticity matrix, T is the stress tensor, e is the piezoelectric couling matrix, $\boldsymbol{D}$ is the electric displacement tensor, ε is the electrical permittivity, and $\boldsymbol{E}$ is the electrical field. The *Electric Currents in Layered Shells* interface solved the governing equation that accounts for both conduction and displacement currents:

$$-\nabla_t \bullet d((\sigma + j\omega\varepsilon_0)\nabla_t V - (\boldsymbol{J}_e + j\omega \boldsymbol{P})) = dQ_j$$

where d is the thickness of the shell, σ is the electrical conductivity, $\boldsymbol{J}_e$ is the external generated current density, Q_j is the external current source, $\boldsymbol{P}$ is the polarization vector. The operator ∇_t represents the tangential derivative along the shell. The *Piezoelectricity, Layered Shell* multiphysics interface provided the linkage between the mechanical and electrical domains within the layered shell formulation. The *Electric Circuit* interface was used to evaluate the output voltage as a function of the piezoelectric layer impedance. By Finite Element Analysis (FEA) simulations, the optimal combination of proof mass, silicon membrane diameter and annular piezoelectric ring width that maximizes the on-axis sensitivity within the operating bandwidth of the accelerometer was identified. Fig. 1 depicts the 2D model geometry of the accelerometer, showing the main components of the device.

Typically, an accelerometer should be designed with the first fundamental resonance frequency at least three times higher than its operating bandwidth to minimize resonance effects, ensure stability in dynamic environments, and improve the linearity and signal-to-noise ratio within the operating range. Since the device has to operate under accelerations between 0.6 and 1.6 g with frequency in the range 0.3–1.2 kHz, its fundamental resonance frequency has to be higher than 3.6 kHz (about three times the bandwidth) [28]. However, it is worth to consider that the on-axis sensitivity in the operating bandwidth tends to decrease as the resonance frequency of the accelerometer increases. Simulations allowed to design the accelerometer for optimizing the performance and minimizing the footprint. Eigenfrequency and frequency domain analyses were performed on a 3D model by varying: i) the proof mass volume, between 7.7 and 8.3 mm^3, ii) the silicon membrane diameter, between 5.1 and 5.5 mm, and iii) the width of the piezoelectric ring, in the range 150–300 μm. The effect of mechanical and piezoelectric coupling losses on the accelerometer performance was also considered. In all the simulations, a mechanical isotropic loss factor of 0.10 was modeled as a minimum value of significant damping. Piezoelectric coupling losses varying in the range 0.02–0.10 were considered in addition to the mechanical damping for evaluating the performance of the optimal accelerometer, in terms of mean output voltage in the operating bandwidth and on-axis sensitivity, under accelerations comprised in the range 0.6–1.6 g. Table 1 reports the properties of the materials used in the simulations.

2.2. Fabrication process

Using standard MEMS techniques, we have developed a fabrication process to realize the proposed device, as shown in Fig. 2. It includes photolithography, thin film deposition and etching process steps.

As shown in Fig. 2, the selected substrate (a) is Silicon-on-insulator (SOI), a wafer substrate consisting of a single crystalline siliconsilicon layer (10 μm-thick) separated from the bulk substrate (400 μm-thick) by a thin buried layer (1 μm-thick) of thermal silicon oxide (SiO_2). This technological choice allows for the minimization of the substrate leakage and eliminate cross talk between circuits. The first layer defined

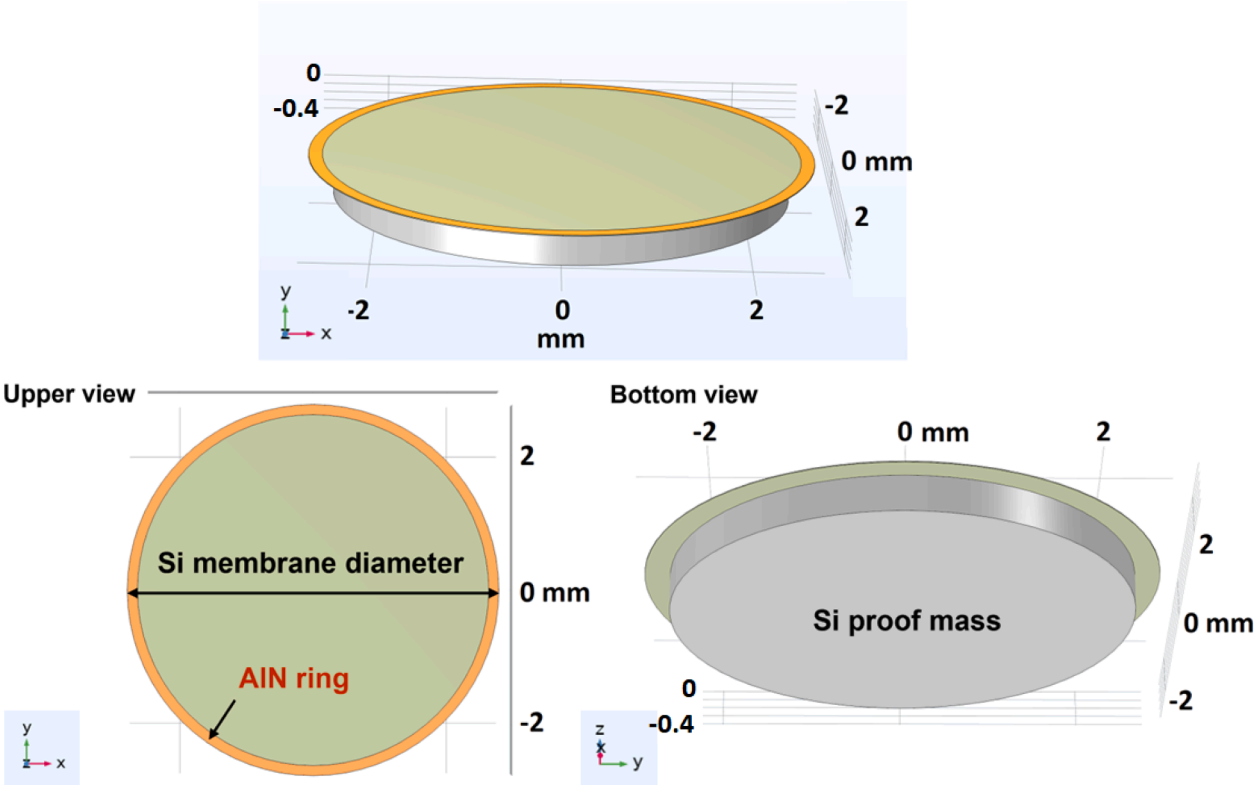

Fig. 1. 2D model geometry, showing the main components of the accelerometer, including the AlN piezoelectric ring, proof mass and membrane size.

Table 1
Materials properties used in the simulations.

Material Properties	
Si [29]	$\rho = 2.33$ g/cm^3; Orthotropic material properties Young's modulus $E_x = E_y = E_z = 130$ GPa Poisson's ratio $\nu_{yz} = \nu_{zx} = \nu_{xy} = 0.28$ Shear modulus $G_{yz} = G_{zx} = G_{xy} = 79.6$ GPa
SiO_2 [30]	$\rho = 2.2$ g/cm^3; E = 70 GPa; $\nu = 0.17$
Ti [31]	$\rho = 4.51$ g/cm^3; E = 100 GPa; $\nu = 0.34$
AlN [28]	$\rho = 2.70$ g/cm^3; $\varepsilon_{ii} = 9$, $\varepsilon_{ij} = 0$ *Elasticity matrix coefficients (GPa)* $C_{11} = C_{22} = 345$ $C_{12} = 125$ $C_{13} = C_{23} = 120$ $C_{33} = 395$ $C_{44} = C_{55} = 118$ $C_{66} = 110$ *Coupling matrix coefficients* (C/m^2) $e_{24} = e_{15} = -0.48$ $e_{31} = e_{32} = -0.58$ $e_{33} = 1.55$

by photolitography is the bottom electrode (b). Titanium (Ti) thin film 200 nm-thick was deposited by sputtering, followed by lift-off process to remove the excess metal and photoresist; the RF power applied to the Ti target was equal to 200 W and the Ar pressure in the chamber was fixed at 2.5 x 10^{-2} mbar, as alreadly largely discussed in an our previuos work [32]. A second photolitography step allows for the outlining of piezoelectric area; then, AlN thin film with a thickness equal to 500 nm was grown by reactive RF magnetron sputtering by applying an RF power of 150 W to the Al target [31] (c). After the definition of the top electrode by photolitography, the deposition of a Ti thin film followed by lift-off (d), and the deep etching of the silicon handle layer by Inductively Couple Plasma (ICP) Etcher process down to the buried silicon oxide which acts as etch stop layer (e), the front structure of the accelerometer was protected by a polymeric film (f) before starting the backside pattern process. The backside fabrication starts with the definition and the etching of silicon proof mass (handle wafer) by ICP (g) while buried silicon oxide etch stop layer was removed by wet etching in BOE (Buffered Oxide Etchant) and (h). Finally, the suspended structures are released by etching the front protective coating (i), completing the fabrication of the accelerometer, shown in Fig. 3.

2.3. Piezoelectric characterization of the device

The fabricated devices were characterized by using the experimental setup sketched and photographed in Fig. 4.

It includes a miniature electrodynamic shaker (Model K2007E007–PCB PIEZOTRONICS) equipped with a calibrated commercial accelerometer used as reference (Model: 352C22–PCB PIEZOTRONICS), a power amplifier (Model 2100E21-100 – PCB PIEZOTRONICS), a function generator and a digital oscilloscope to record the Device Under test (DUT) output signals. Piezoelectric elements produces some picocoulombs of charge in one working cycle, whose amount can be measured by a charge amplifier. To this aim the experimental set-up was equipped with an in-line charge converter (PCB Piezotronics – 422E5x) with a high internal load resistance (120 GΩ). The instrument converted the high-impedance signal produced by the piezoelectric element into a measurable low-impedance signal. Low-noise cables were necessary to reduce both the charges generated by cable motion (triboelectric effect) and the noise caused by radio frequency and electromagnetic interferences. A voltage amplifier (FEMTO DLPVA 100-F-S) was used to measure the voltage generated by the accelerometer when mechanically deformed. It was characterized by an extremely high input impedance equal to 1 TΩ such to consider the input current approximately zero. Thus, it can be used as buffer to link

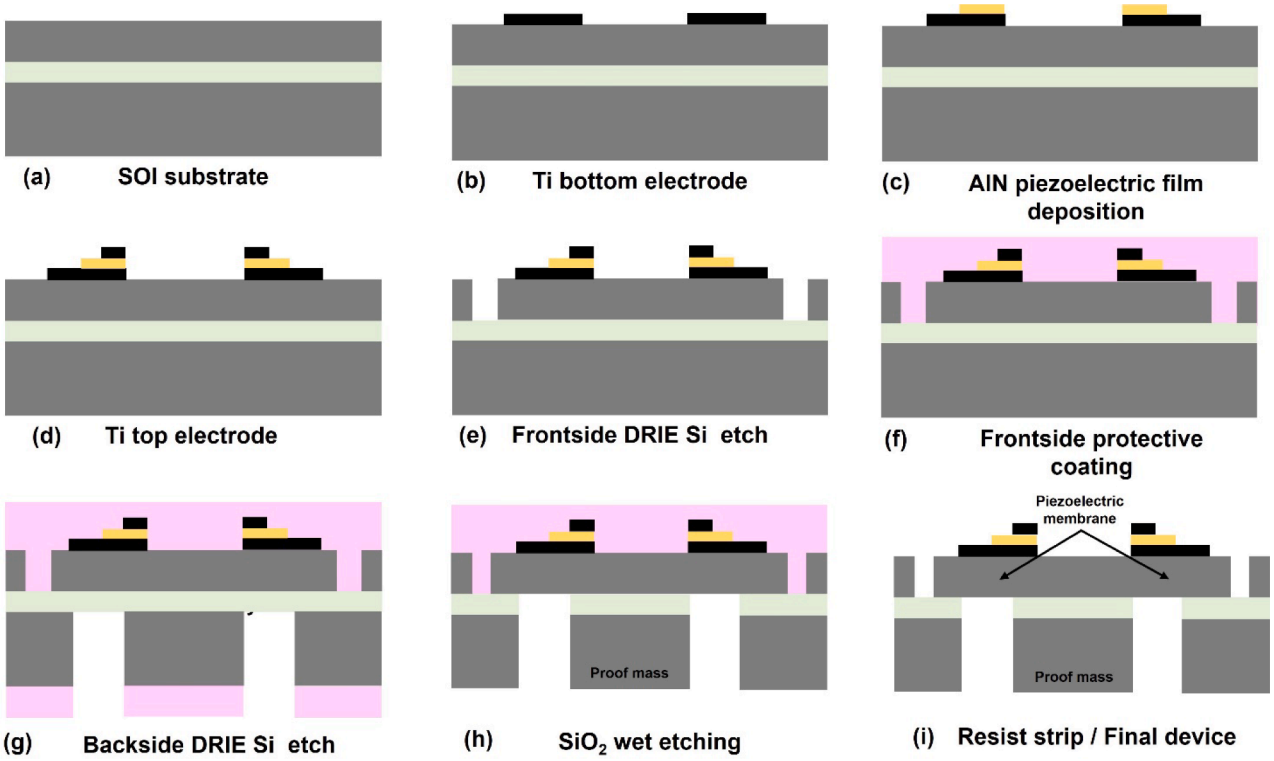

Fig. 2. From (a) to (h) flowchart of the experimental steps followed for the fabrication of the mems piezoelectric accelerometer. The entire fabrication process was carried out in the Advanced Micro And Nano DEvices laboratory (AMANDe Lab) at the Institute for Miroelectronics and Microsystems in Lecce.

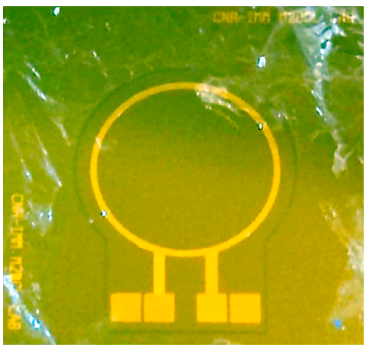

Fig. 3. Image of the fabricated piezoelectric accelerometer.

piezoelectric accelerometer output to the oscilloscope for the evaluation of the generated voltage.

2.4. Nanomechanical characterization of the piezoelectric thin film

The AlN film used as the active layer in the proposed accelerometer, deposited according to the optimized sputtering conditions that guarantee suitable crystallographic orientation and piezoelectric response, as reported elsewhere [33], was subjected to nanoindentation measurements to investigate its nanomechanical properties. Nanoindentation was performed on a film 0.5 μm thick using a nanoindenter (Anton Paar mod. TTX-NHT2) equipped with a Berkovich diamond tip, following the international standard ISO 14577. Load-displacement characterization was performed in load control mode at constant loading/unloading rates of 4 mN/min and maximum load of 2 mN, resulting in a maximum penetration depth of about 75 nm. Preliminary tests were conducted by setting a 30 s hold time both at the maximum load and at a low load (i.e. 10 % of maximum load) to account for any creep or thermal drift phenomena, respectively, both resulting at an acceptable level below 5 % during the measurements. Poisson's ratio of 0.21 for wurtzite aluminum nitride [34,35] was used for the Oliver and Pharr analysis of the unloading curves to obtain instrumented indentation hardness H_{IT} and elastic modulus E_{IT} values. Several regions of the film surface were sampled by nanoindentation measurements to exclude disuniformity of the values over the surface, arranging a set of 10 indentations, separated by 20 μm within the indentation set in each region, and then calculating the average values of H_{IT} and E_{IT}.

2.5. Test set-up for combustion monitoring

The microfabricated piezoelectric accelerometer was characterized under realistic working conditions at the Green Engine Laboratory of the University of Salento. For this purpose, a high-performance 300-kW liquid-fueled swirled combustor was employed, featuring a cylindrical combustion chamber with an internal diameter of 4 cm and a length of 29 cm. A schematic diagram of the combustion chamber, including the positioning of the piezoelectric accelerometer, is presented in Fig. 5.

The combustion system's airflow was delivered to the chamber through a dual-flow mechanism using concentric annular tubes, allowing for optimized mixing of fuel and air. The inner passage is equipped with a fixed-geometry axial swirler, consisting of eight vanes inclined at 45°. This configuration imparts significant angular momentum to the inner air stream, playing a key role in flame stabilization by promoting internal recirculation and enhancing air–fuel mixing. Based on the swirler geometry and the dimensions of the flow passages, the swirl number was calculated to be approximately 0.67, which is a typical value for inducing the formation of an axial flow recirculation zone. The Jet-A1 was injected into the combustion chamber at 7 bar, with an injection angle of 45°. The fuel mass flow rate was monitored with a precision of ± 2 % of the reading, while the air mass flow rate was estimated with an accuracy of ± 1 % of the full-scale value (f.s.v.). To monitor the combustion phenomenon, a highly accurate Kistler PiezoSmart Type 4045A2 pressure sensor was located near the flame and cooled to keep the local temperature below 413 K which is the maximum declared operating limit. The fabricated accelerometer was placed on the structure of the combustion chamber in a position such to be more sensitive to combustion-related vibrations and less to other noise sources. The signals coming from both sensors have been elaborated through variance and Kurtosis data analysis techniques to achieve quantitative information about combustion instability [36].

3. Results and discussion

3.1. Nanomechanical characterization of the active layer of the accelerometer

The evaluation of the mechanical properties of the active thin films is

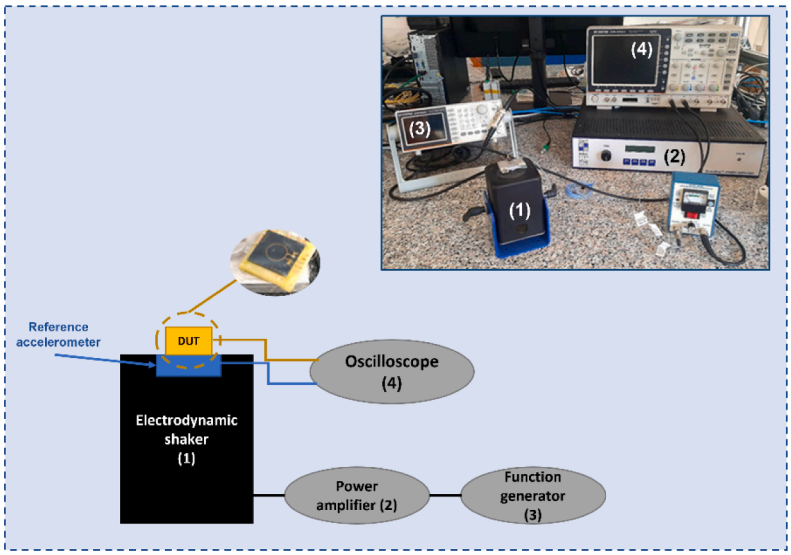

Fig. 4. Schematic representation of the experimental set-up used for the functional characterization of the piezoelectric accelerometer; in the inset, the photo of the experimental bench set-up in the multifunctional and devices design and characterization laboratory (m2dcl) at the institute for miroelectronics and microsystems of lecce.

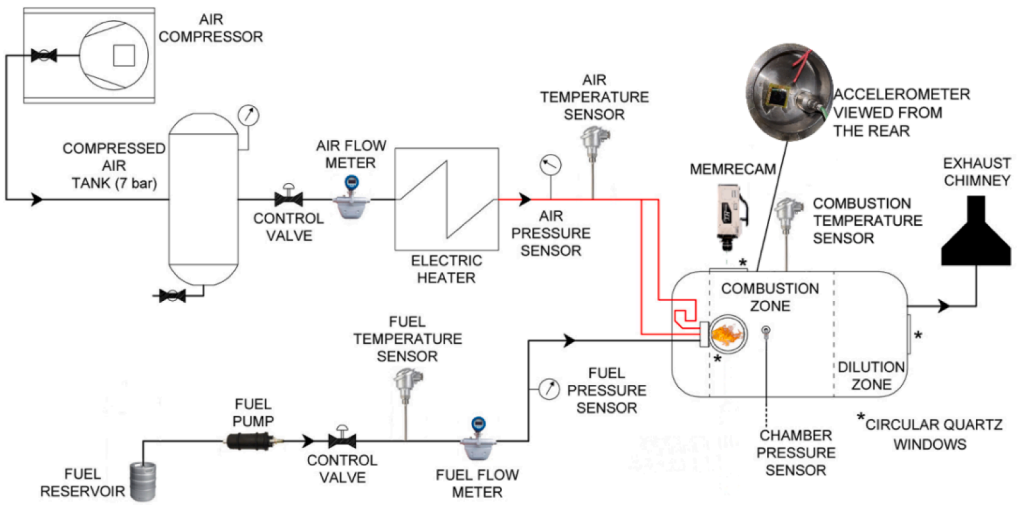

Fig. 5. Green Engine combustion chamber set-up diagram at Green Engine Laboratory of the University of Salento. (For interpretation of the references to colour in this figure legend, the reader is referred to the web version of this article.)

indispensable for designing piezo-MEMS devices, since they play a key role for the device performance and reliability. Fig. 6 displays an excerpt of ten load–displacement curves from the nanoindentation characterizations on the AlN surface.

The average values of instrumented nanohardness and elastic modulus derived from the analyses are, respectively:

- $H_{IT} = (20 \pm 3)$ GPa
- $E_{IT} = (211 \pm 18)$ GPa

The hardness value is comparable to those reported for sputtered AlN films in previous works [37–39] despite the room temperature process adopted in our work instead of the higher substrate temperatures used in other works. At the same time, the assessed value of the elastic modulus is lower than values found on other AlN films (approximately in the range 230–280 GPa) [40,41] and bulk wurtzite AlN (290–380 GPa) [42], thus suggesting a slightly more elastic behavior in our material. This can be also inferred from the narrow shape of the load–displacement curves, quantitatively expressed by the percentage η_{IT} of the elastic work, defined as (1):

$$\eta_{IT}(\%) = \frac{W_{elast}}{W_{total}} \times 100 \quad (1)$$

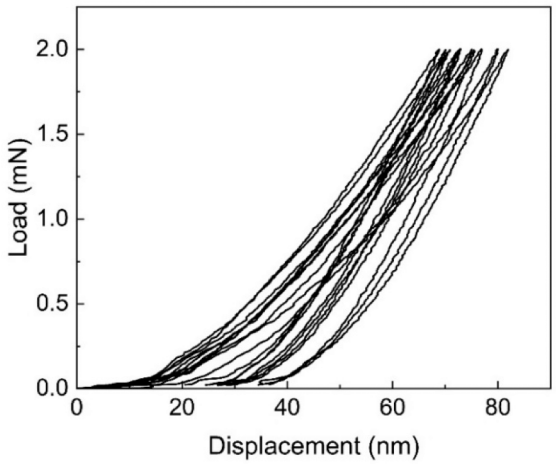

Fig. 6. Set of load–displacement curves obtained from the nanoindentation measurements on AlN film.

where $W_{total} = W_{elast} + W_{plast}$ is the total mechanical work done during the application of the indentation force (corresponding to the total area under the loading curve of the load–displacement graph), being W_{plast} the work consumed as plastic deformation of the material during the load application and W_{elast} the remaining part of the work related to the elastic recovering of the material during the load removal (corresponding to the area under the unloading curve of the load–displacement graph). The average value of η_{IT} resulting from our nanoindentation analyses is (70 ± 3) %, thus indicating that about 30 % of the work induced a plastic deformation of the material during the load application while 70 % is recovered by the elastic reversion of the material upon load removal. The behaviour prevalently elastic of our AlN thin film could be beneficial for the mechanical characteristics of our device.

3.2. *Validation of the performance of the piezoelectric accelerometer: Comparison between simulation results and experimental data*

As already reported in the experimental section, simulations allowed to optimize the performance of the designed device by considering different cases of study. The first one explored the change of resonance frequency with the Si membrane diameter and proof mass volume, with the width of the piezoelectric ring considered constant and equal to 150 μm. The results showed that the proof mass volume is the factor that significantly influences the device's resonance, while the change due to the Si membrane diameter is minimal (Fig. 7). The resonance frequency of Si membranes with added mass of 7.7 mm^3 is approximatively 4 kHz, and increases with bigger proof masses due to the annular shape of the vibrating element. To maximize the on-axis sensitivity of the accelerometer in the operating bandwidth, the design was optimized by seeking within the framework of low-resonance solutions, which allow to maximize the sensitivity in the operating bandwidth.

The output voltage of the three membranes with resonance frequency around 4 kHz was evaluated as a function of the width of the piezoelectric ring. The latter covers the high strain regions near the membrane clamped edges to enhance the conversion of mechanical deformation into electrical energy. However, as the ring width increases, the impedance of the AlN layer rises, reducing the device's output voltage. Fig. 8 shows the mean output voltage at 1 g in the bandwidth 0.3 – 1.2 kHz for piezoelectric ring width between 150 and 300 μm. The best performance is obtained by a 5.5 mm-wide Si membrane with a 150 μm-wide piezoelectric ring, coupled to an added mass of 7.7 mm^3.

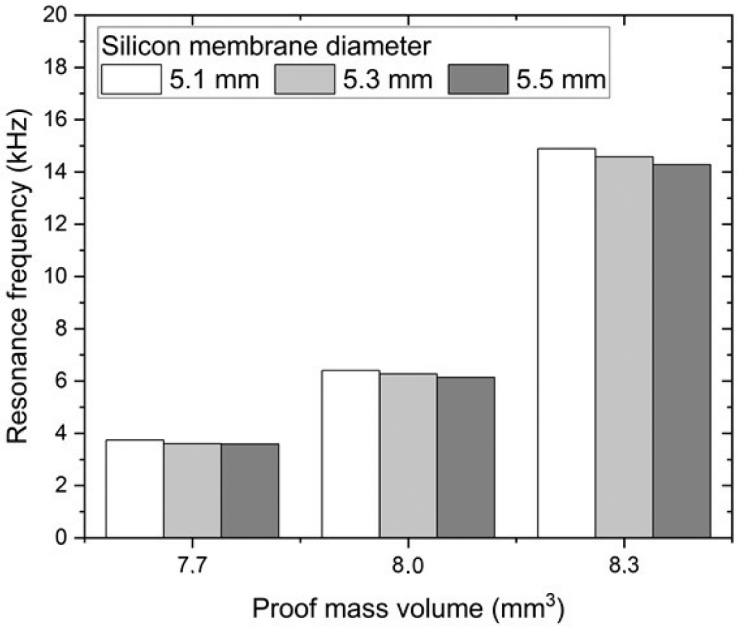

Fig. 7. Simulated resonance frequency of the accelerometer for increasing proof mass volume and Si membrane diameter.

Fig. 9 shows the output voltage at 500 Hz in the range 0.6 g − 1.6 g, with increasing piezoelectric coupling losses in addition to the mechanical ones. The comparison revealed a significant reduction in output voltage for coupling losses ranging from 0.02 to 0.10, which reflects in the on-axis sensitivity decrease from 1.99 mV/g, with only mechanical losses, to 0.17 mV/g with an additional coupling loss of 0.10.

To validate simulation results, the microfabricated accelerometer was characterized in terms of frequency response (to extract the resonance frequency) and sensitivity. The working frequency response was studied in the frequency range from 0.3 – 5 kHz at 1 g, as shown in Fig. 10. The bandwidth of the DUT is defined as the Full Width at Half Maximum (FWHM) value of the voltage versus frequency graph. The Q-factor of the piezoelectric accelerometer can be calculated as the ratio between the resonant frequency and the bandwidth at half the peak voltage: $Q = \frac{f_{res}}{\Delta f_{0.5V}}$. The total damping ratio ξ (mechanical and electrical) can be obtained from the formula: $\xi = \frac{1}{2Q}$ [43] [$\xi = \xi_e$ (electrical damping ratio) + ξ_m (mechanical damping ratio) = $c/2mf_{res}$ where c is the damping coefficient]. The Lorentzian fitting results are shown in Fig. 10.

A good flatness in the response is observed between 300 Hz and 1.2 kHz (working frequency band) and the resonance frequency results to be peaked at 3.8 kHz, coherently with COMSOL simulation results, considering the negligible shift towards lower frequency due to known effects strictly related to fabrication process [44]. To evaluate the degree of accuracy of the measurement in the working frequency band, four acquisitions at discrete frequency in the flat band were recorded, in four different days (one for each measurement day) at 1 g of acceleration.

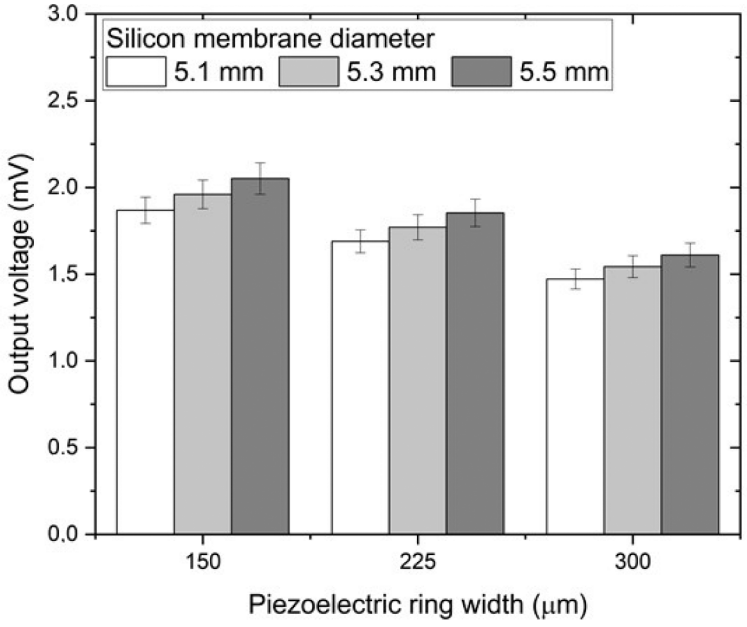

Fig. 8. Mean output voltage in the operating bandwidth at 1 g acceleration, for increasing Si membrane diameter and piezoelectric ring width (added mass of 7.7 mm^3).

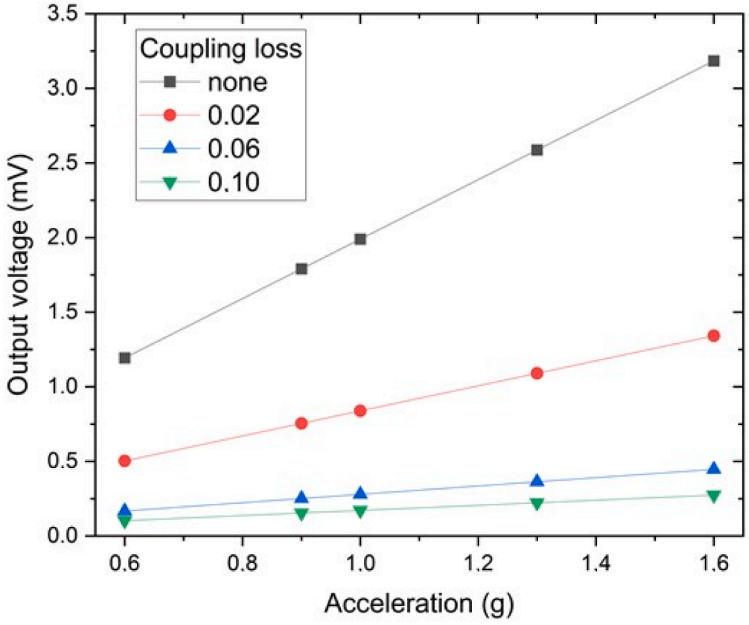

Fig. 9. Output voltage at 500 Hz vs acceleration for increasing piezoelectric coupling loss.

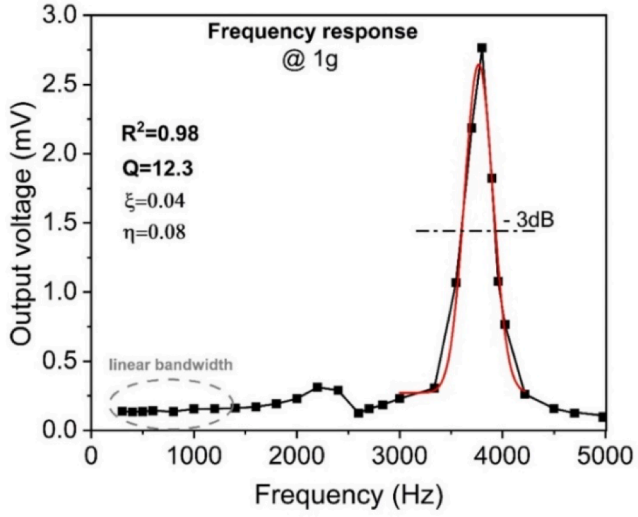

Fig. 10. Frequency response from 300 Hz to 5 kHz at @1g acquired from the functional characterization of the fabricated piezoelectric accelerometer. The results of the fitting procedure on frequency response of the DUT to evaluate Q-factor, loss factor and dumping ratio are also shown.

Table 2 summarizes the measured output voltage values. The minimization of the noise is a key issue for some practical applications of the accelerometers, especially when the detection of low-amplitude vibrations is required (i.e. seismic or industrial applications). In this specific case, the input signal can be masked by noise and, consequently, it is not detected, reducing the sensitivity of the accelerometer.

The average value of the accelerometer output (average transmissibility) in the flat frequency range is (0.151 ± 0.008) mV/g. In other words, the average measurement inaccuracy is equal to 5 %. This result is summarized in Fig. 11(a). Fig. 11(b) shows the trend of the measurements performed each day in the flat band frequency region. To corroborate the accuracy evaluation, the frequency response of the accelerometer was measured in the flat band for three times at different accelerations, i.e. 0.6 g, 0.8 g and 1.5 g, and normalized with respect to each acceleration taken into account, as shown in Fig. 11(c). The trends confirm a high degree of accuracy of the measurements.

The sensitivity of the accelerometer is defined as the voltage or charges generated per applied acceleration. To study the sensitivity and the linearity of the piezoelectric accelerometer, the open circuit voltage and the open circuit output charge were extracted by the voltage amplifier and the in-line charge converter, respectively, at accelerations spanning from 0.6 g to 1.6 g at the vibration frequency of 500 Hz, as reported in Fig. 12.

The voltage sensitivity S_v was obtained from the slope of the linear fitting of the experimental data shown in Fig. 12a, resulting equal to 0.25 mV/g. This is in good accordance with simulation results in which an additional coupling loss to the mechanical one, ranging between 0.06 and 0.10, was considered. This was done to attribute piezoelectric material losses in MEMS devices [45]. Simulations provided a sensitivity range of 0.17–0.28 mV/g (Fig. 9). Linear regression gave R^2 value equal to 0.99, confirming the great linearity of the piezoelectric MEMS

Table 2
Output voltage of the accelerometer for 4 different measurements at @1g.

Frequency (Hz)	Meas 1 (mV/g)	Meas 2 (mV/g)	Meas 3 (mV/g)	Meas 4 (mV/g)	Average value (mV/g)	STD	Relative error (%)
300	0.150	0.155	0.138	0.140	0.146	± 0.008	5.5
400	0.155	0.155	0.135	0.140	0.146	± 0.010	7.0
500	0.165	0.158	0.137	0.140	0.150	± 0.014	9.2
600	0.160	0.160	0.147	0.150	0.154	± 0.007	4.5
700	0.160	0.160	0.137	0.145	0.150	± 0.012	7.7
800	0.155	0.155	0.150	0.140	0.150	± 0.007	4.7
1000	0.160	0.160	0.155	0.150	0.156	± 0.005	3.1
1200	0.160	0.158	0.154	0.150	0.156	± 0.004	2.5

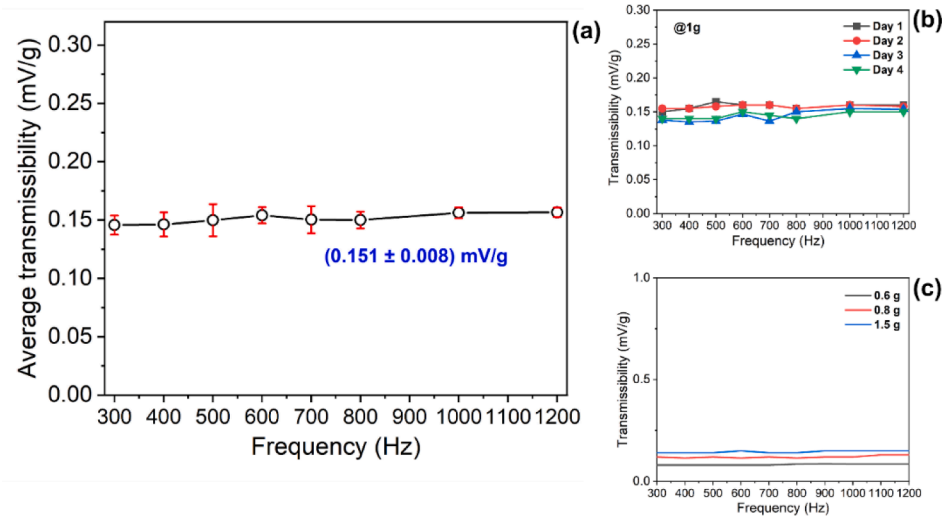

Fig. 11. (a) average transmissibility of the accelerometer in the working bandwidth; (b) trend of the measurements performed each day in the flat band frequency region; (c) transmissibility of the accelerometer in the working bandwidth at three different acceleration values.

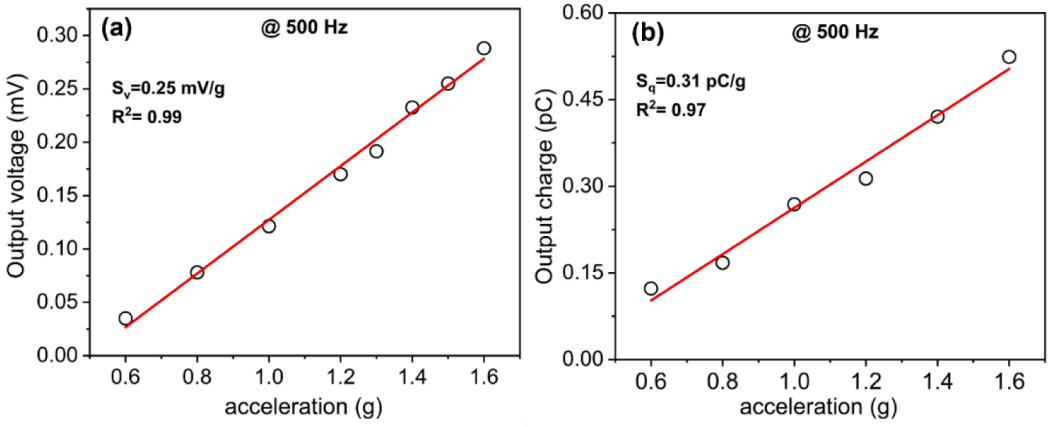

Fig. 12. A) output voltage and (b) output charge versus acceleration. The voltage sensitivity and the charge sensitivity of the microfabricated accelerometer were obtained as the slope of the linear fitting of the data (red line) and indicated in the graphs. (For interpretation of the references to colour in this figure legend, the reader is referred to the web version of this article.)

accelerometer. Analogously, the charge sensitivity S_q was obtained from the the slope extracted from the graph of the output charges versus acceleration, shown in Fig. 12b, resulting equal to 0.31 pC/g. Linear regression gives R^2 value equal to 0.97, confirming the good linearity of the piezoelectric MEMS accelerometer. All the experimental parameters obtained through the previous characterization allowed for the calculation of the noise which affects the device response. As largely known, piezoelectric accelerometer is mainly made of two functional parts: a mechanical damped harmonic oscillator and an electrical-thermal part made of the piezoelectric material which generates electric charges proportionally to the mechanical movement. Both contribute to noise generation (mechanical and electrical) which constitutes the total noise of the transducer. Specifically, mechanical noise can be related to the mass, to the spring constant, and to the mechanical resistance of the sensor's seismic system. Electrical-thermal noise is an additional noise caused by any internal or external electronics used in the measurement system. It is a function of the sensing materials loss factor which is the inverse of the materials quality factor. Following the work of F. A. Levinzon [46], mechanical and electrical acceleration noise spectral density, indicated as a_{nm} and a_{ne}, respectively, can be evaluated by considering the following formulas:

$$a_{nm} = \sqrt{\frac{4k_B T\omega_0}{mQ}}a_{ne} = \sqrt{\frac{4k_B T\eta C}{\omega S_q^2}} \quad (2)$$

where k_B is the Boltzmann's constant (1.38×10^{-23} J/K), T is the absolute temperature, the angular frequency $\omega_0 = 2\pi f_0$, where f_0 is the first resonance frequency, m is the mass of the accelerometer, Q is its quality factor, η=2ξ is the dissipation factor of the piezoelectric material, C is the electrical capacitance of the piezoelectric material, $\omega = 2\pi f$, where f is the excitation frequency, and S_q is the charge sensitivity. Mechanical noise equivalent acceleration a_{nm} is an invariant with respect to frequency when $f << f_0$ (as in this case where $f = 500$ Hz$<< f_0 = 3800$ Hz). a_{nm} and a_{ne}, both generate a voltage noise spectral density at the output of the transducer, indicated as v_{nm} and v_{ne}:

$$v_{nm} = a_{nm} \bullet S_v$$

$$v_{ne} = a_{ne} \bullet S_v$$

where S_v is the voltage sensitivity.

To obtain the values of noises through equations (2), the electrical capacitance C of the transducer must be calculated. It was experimentally found by considering the structure reported in Fig. 13. The

capacitor is made of two Ti electrodes with AlN 500 nm-thick film sandwiched inside.

Specifically, the bottom electrode is made of a continuous Ti thin film 200 nm-thick while top electrode was realized by lithography technique being arranged into Ti pixel shape with a diameter of 200 μm and a thickness of 200 nm, too. Capacitance *C* can be calculated by the following formula:

$$C = \epsilon_0 \varepsilon_r \frac{A}{d}$$

where $\varepsilon_0 = 8.85 \cdot 10^{-12}$F/m, ε_r is the dielectric constant of AlN thin film, A $= 2.52 \cdot 10^{-6}$ m^2 (electrode area) and d $= 5 \cdot 10^{-7}$ m (AlN thickness). The dielectric constant evaluation was made by capacitance measurements in frequency range from 20 Hz to 1 MHz. The resulting value was $\varepsilon_r = 10.25 \pm 0.25$. As a consequence, C resulted to be equal to 457 pF at 1 kHz. This is an approximated value considering that very small capacitances are also associated with probes and cables (usually in the region of few pF [47]) that now we neglected being the film capacitance significantly higher in value. Table 3. Summarizes the experimental parameters used for the calculation of a_{nm} and a_{ne}.

The total noise a_{tot} of the accelerometer can be calculated by adding both noise components and it is equal to 41 $\frac{\mu g}{\sqrt{Hz}}$ at 500 Hz. The noise power spectral density P_{SD} of the sensor is given by the following formula:

$$P_{SD} = \sqrt{a_{nm}^2 + a_{ne}^2}$$

and it is practically equal to 41 $\frac{\mu g}{\sqrt{Hz}}$. The total fundamental noise limit is determined basically by the electrical-thermal noise of the transducer which generally dominates [46]. The voltage electrical-thermal noise spectral density at the output of the transducer resulted to be equal to 10.2 $\frac{nV}{\sqrt{Hz}}$. Table 4 compares noise and other parameters of our accelerometer with some single-axis commercial accelerometers generally used for the vibration measurement of gas-turbine engines for aircraft and industrial applications. The noise is comparable with the values reported for commercial accelerometers. The minimization of the noise is a key issue for some practical applications of the accelerometers, especially when the detection of low-amplitude vibrations is required (i.e. seismic or industrial applications). In this specific case, the input signal can be masked by noise and, consequently, it is not detected, reducing the sensitivity of the accelerometer.

3.3. Characterization of the accelerometer in working conditions

As detailed in the experimental setup, the characterization of the piezo-MEMS accelerometer under realistic working conditions was conducted through experimental tests of self-induced combustion instability using Jet-A1 fuel. Preheated inlet air at a temperature of 410 K was used. The air was preheated to 410 K to simulate realistic operating conditions typical of aerospace combustors, where compressed air can reach high temperatures due to isentropic compression in the compressors. This value is frequently adopted in tests on premixed and non-premixed combustors, as it ensures stable ignition of Jet-A1 fuel and promotes the onset of self-induced instabilities, without exceeding the critical temperature limits of the experimental components [48,49]. The air mass flow rate was fixed at two different values, 40 g/s and 80 g/s, while keeping the fuel mass flow rate constant at 1.00 g/s. This value of the fuel mass flow rate was adopted to simplify the comparative analysis, allowing a controlled variation of the global equivalence ratio by varying only the air mass flow rate. This approach is in line with common practices in unstable combustion tests near the lean blowout limit [50,51]. The equivalence ratios (Φ) close to Lean Blowout (LBO) can be calculated following the formula:

$$\Phi = \left(\frac{\dot{m}_f}{\dot{m}_a}\right) / \left(\frac{\dot{m}_f}{\dot{m}_a}\right)_{st}$$

where $\dot{\boldsymbol{m}}$ represents the mass flow rate and the subscripts ***f*** and ***a*** indicate the fuel and air flows, respectively, while ***st*** denotes stoichiometric conditions with a stoichiometric fuel/air ratio of 1:14.5. For air mass flow rates of 40 g/s and 80 g/s, the equivalence ratios were determined to be 0.36 and 0.18, respectively. These signals were then analysed comparatively to underline, by means of correlation, the dynamic relation of pressure fluctuation with the vibration induced by combustion. Then, statistical metrics such as mean, variance, and kurtosis of the temporal signal in both equivalence ratio test cases were used to characterize the instability regimes of the phenomenon. These analyses provided insight into amplitude and variability of instabilities and proved the effectiveness of the accelerometer in the detection of combustion-induced vibrations. Fig. 14 highlights the capability of the piezo-MEMS sensor (top) to detect dynamic fluctuations associated with combustion, showing behavior consistent with that measured by the commercial pressure sensor (bottom). The MEMS signal faithfully reproduces the main temporal characteristics of the pressure field, demonstrating the device's potential for monitoring instabilities under real operating conditions.

At a global equivalence ratio of $\phi = 0.18$, the air–fuel mixture is very lean and under these conditions, the reaction time increases, and the flame becomes particularly sensitive to velocity and pressure fluctuations. This sensitivity can lead to unstable flame behaviour which, although close to blow-off, may undergo a phase of pronounced thermoacoustic instability. Lean conditions, in fact, promote coupling between acoustic oscillations in the combustion chamber and the flame response, amplifying pressure fluctuations. Conversely, at $\phi = 0.36$, the mixture is richer, and the flame is more stable and less prone to self-excited oscillations. In this regime, combustion is more robust and tends to acoustically dampen perturbations, reducing both transmission and amplification of pressure fluctuations [52].

Fig. 15 depicts the dynamic correlation coefficient (DCC) between the two sensors signals over time. The data are sampled at a frequency of 10 kHz.

The DCC quantifies the temporal degree of correlation between pressure and acceleration signals, offering insight into aeroelastic coupling in the chamber. It is to be noted that the DCC values fluctuate within a bounded range from 0.9964 to 0.9982 for both equivalence ratios, showing the strongly and persistently correlated two signals during the measurement period.

Theoretically, the DCC ranges between −1 and 1, where:

- DCC = 1 implies a perfect positive correlation, meaning the two signals evolve in sync.
- DCC = −1 indicates a perfect negative correlation, where the signals exhibit inverse behavior.

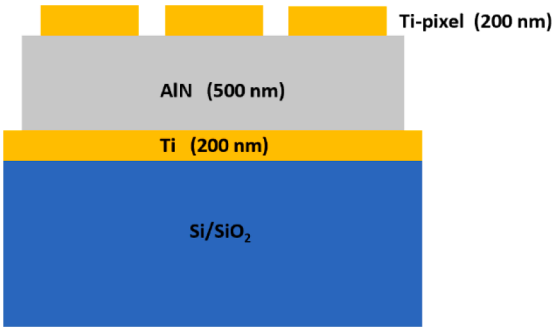

Fig. 13. Fabricated structure for the evaluation of capacitance C of the piezoelectric AlN thin film.

Table 3
Experimental parameters used for the calculation of a_{nm} and a_{ne}.

T (k)	ω_0(Hz)	ω(Hz)	m (mg)	C (pF)	S_q (pC/g) @500 Hz	Q	η	a_{nm} ($\frac{\mu g}{\sqrt{Hz}}$)	a_{ne} ($\frac{\mu g}{\sqrt{Hz}}$) @500 Hz
297	$23.9 \cdot 10^3$	3140	19.8	457	0.31	12.3	0.08	**0.04**	**41**

Table 4
Comparison with commercial piezoelectric accelerometer suitable for gas-turbine engines vibration monitoring.

Accelerometer model	Noise density ($\frac{\mu g}{\sqrt{Hz}}$)	Resonance frequency (KHz)	Technology	Application
ADXL 1001	30 @ 1 Hz	21	Piezoelectric MEMS	• Condition monitoring • Predictive maintenance • Health usage monitoring sytems
ADXL 1005	75 @ 100–20 kHz	42	Piezoelectric MEMS	• Condition monitoring • Predictive maintenance • Asset health • Acoustic emissions
Endevco 6222	Low noise (not declared)	45	Piezoelectric	• vibration measurement of gas-turbine engines
EX611A20	Low noise (not declared)	> 17 KHz	Piezoelectric No built-in microelectronics	• structural testing • machine monitoring • high temperature machinery vibration measurement.
Our work	41 @500 Hz	3.8	Thin film-piezoelectric MEMS No built-in microelectronics	• COMBUSTION INSTABILITY

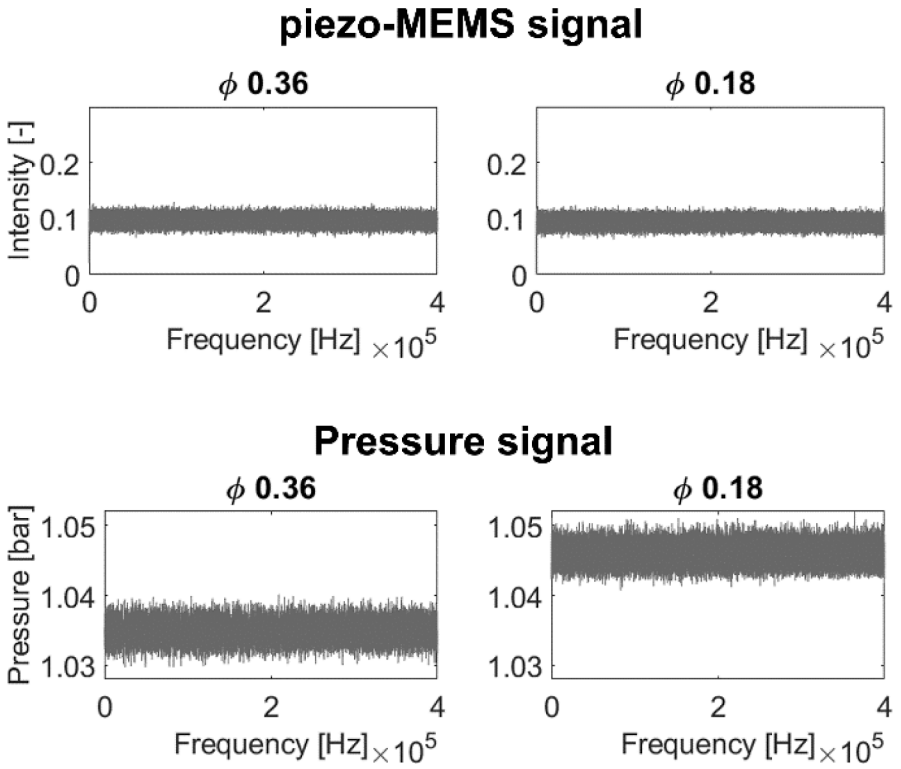

Fig. 14. Comparison of time signals acquired with the piezo-MEMS accelerometer (top) and the commercial pressure sensor (bottom).

- DCC = 0 signifies the absence of correlation, implying that pressure and acceleration signals are independent.

Fig. 15 shows DCC with time for the pressure sensor and the piezo-MEMS accelerometer at two equivalence ratios: Φ = 0.36 is a moderately unstable combustion regime; Φ = 0.18 is a near-LBO condition where the oscillations have considerably lower intensity. In both instances, the DCC remains rather constant at a high level of 0.9964 to 0.9982. This suggests a very strong correlation in the pressure and acceleration signals measured. However, one can notice an important difference between the two conditions. At Φ = 0.36, DCC shows larger fluctuations, hence higher variability in the coupling between pressure and acceleration signals. This might suggest that combustion dynamics are more energetic and include more pronounced instability effects. At Φ = 0.18, DCC fluctuations seem smaller and more stable in time. Approaching LBO, pressure and acceleration tend to a correlation that most likely gets stabilized with lower amplitude of oscillations because of reduced energy due to combustion processes. Such a reduced oscillation in DCC could reflect the transition towards the lower energy state just before complete flame extinction. Thus, while Φ = 0.18 corresponds

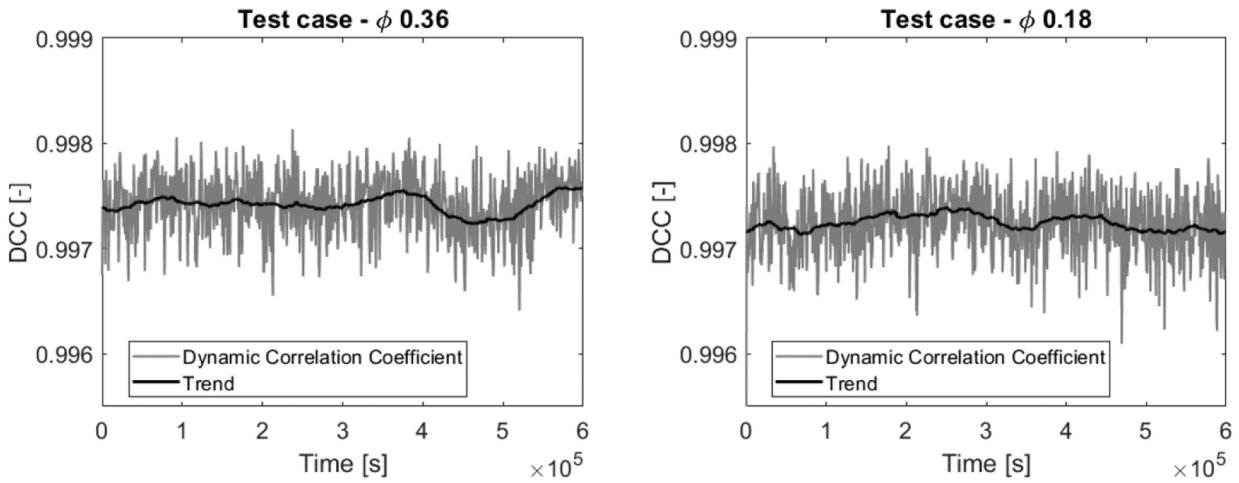

Fig. 15. Dynamic correlation between the time signals of the commercial pressure sensor and the microfabricated piezo-MEMS accelerometer for both test cases, Φ = 0.36 on the left and Φ = 0.18 on the right.

to a regime closer to flame extinction and overall instability, the DCC fluctuations do not increase. This suggests that the instability has transitioned into a more uniform, lower-energy regime, where pressure and structural vibrations remain correlated but with lower intensity variations. Statistical analysis based on mean μ, variance σ^2, and Kurtosis K measurements provides detailed overview of the characteristics of the signals coming from the sensors, useful for understanding the phenomena related to combustion. The variance σ^2 is calculated using the formula:

$$\sigma^2 = \frac{1}{N}\sum_{i=1}^{N}(x_i - \mu)^2$$

where x_i is the instantaneous value, μ is the mean value of the signal, and N is the total number of samples. The kurtosis K is defined as:

$$K = \frac{1}{N}\sum_{i=1}^{N}\left(\frac{x_i - \mu}{\sigma}\right)^4$$

Both definitions follow standard statistical convention as stated in ISO 3534–1:2006 [53]. Fig. 15 and 16 show the statistical probability density distributions from piezo-MEMS and pressure signals, respectively, for two equivalence ratios, ϕ = 0.36 and ϕ = 0.18, to get an insight into combustion dynamics.

Fig. 16a shows the empirical probability density distribution where the histograms of both signals are seen close to Gaussian-like behavior. Therefore, passing from Φ = 0.36 to Φ = 0.18 introduces slight changes in the mean value and in the distribution; that is to say, from 0.0967 the mean of the accelerometer decreases to 0.0932, while from 1.0348 the mean of pressure signal increases up to 1.0460. It is possible to observe that the maximum value of the temporal signal mean corresponds to a different equivalence ratio for each sensor: at Φ = 0.36 for the piezoelectric accelerometer and at Φ = 0.18 for the pressure sensor. Variance is another key metric for evaluating signal dispersion from this figure and, in the context of combustion instability, it reflects the amplitude of fluctuations in pressure and acceleration over time. The comparison between the pressure sensor and the accelerometer variance trends allows for a better understanding of the coupling between combustion-induced pressure oscillations and structural vibrations in the chamber. At Φ = 0.36, the distribution of variance is expected to be wider, showing greater fluctuations in both pressure and acceleration signals. This agrees with the moderately unstable combustion regime, where

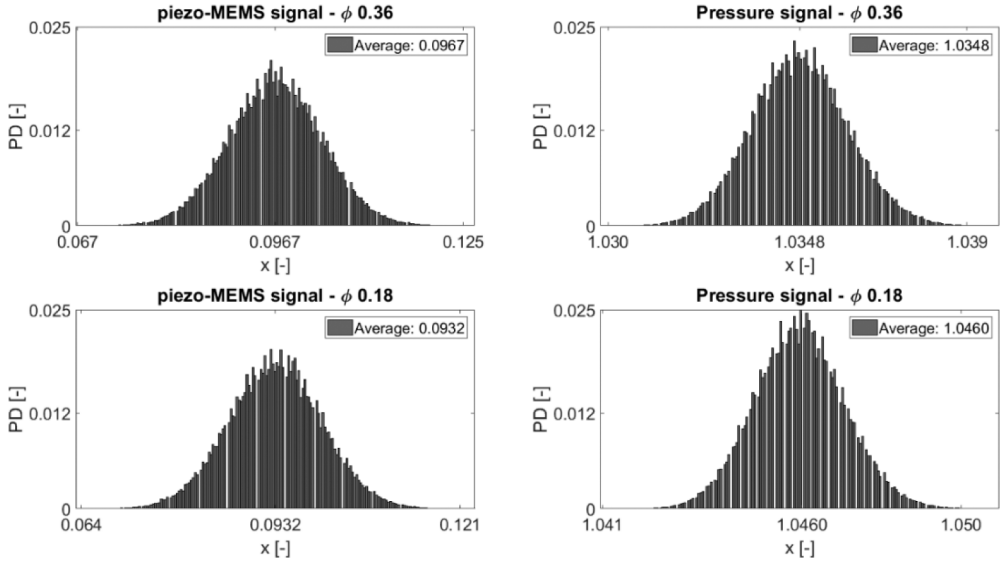

Fig. 16a. Variance trend on probability density scale for the time signals of the commercial pressure sensor and the microfabricated piezo-MEMS accelerometer for both analyzed test cases, Φ = 0.36 and Φ = 0.18.

periodic events of instability lead to noticeable oscillations in pressure and structural vibrations. The MEMS accelerometer follows the trend of the pressure sensor variance and thus confirms its capability to effectively capture combustion-induced mechanical responses. On the other hand, at $\Phi = 0.18$ close to LBO, the variance distribution narrows down, showing a reduction in the amplitude of fluctuations as combustion approaches the blowout threshold. The reduced variance could indicate lower-energy combustion dynamics where the instability-driven oscillations become less intense but may still persist in an intermittent manner. It is also consistent with the previous works, where DCC was high but now with smaller fluctuation (see Fig. 12), which is indicative of the transition to the more uniform regime with lower energy before flame extinction. Directly comparing the output of the two sensors, pressure fluctuations are in good agreement with structural vibrations both for baseline and control configuration. The miniaturized footprint MEMS accelerometer captured the real-time instability-driven variance trends and proved effective, even with the miniaturization of its footprint. With $\Phi = 0.36$, the accelerometer variance is tracking that from the pressure sensor fairly well, which reinforces the fact that most of the influential vibrational modes in the chamber are being strongly linked to pressure oscillations. But for $\Phi = 0.18$, the general variance reduced, whereas subtle discrepancies between the two, suggesting persistence of vibration as pressure fluctuation was being stabilized, were probably an underling of residual mechanical resonant effects of the structure. The normalisation of the probability distributions in Fig. 16b, with respect to their respective mean value, allows a shape-based comparison independent of absolute magnitude.

The piezo-MEMS distributions show smooth and broad characteristics, testifying to a continuing mechanical fluctuation; on the other hand, pressure signals are characterised by sharp peaks around the mean, pointing to a more stable pressure field with only minor deviation. Such a contrast indicates that the two measurement techniques represent different sensitivities: while the transient structural responses captured by the piezo-MEMS sensors are within a wider range, pressure signals still remain more constrained. These findings suggest that at $\phi = 0.36$ the broader distribution of the piezo-MEMS signal and the increased variance in pressure fluctuations could be indicative of higher turbulence levels or increased instability in the combustion process. Conversely, at $\phi = 0.18$, the distributions appear more confined, pointing to a more stable combustion regime. The complementary presentation of both empirical and normalized distributions allows for a comprehensive evaluation of the combustion-induced fluctuations and their potential impact on system stability. Kurtosis is a measure of the sharpness of the peak and heaviness of the tail in the distribution, and it plays an important role in assessing the stability and variability of the recorded signals. Kurtosis values show how much a dataset's distribution is "peaked" or "flat". More precisely, a high value of kurtosis indicates that the data are more extremely peaked than would be the case for a normal distribution. In this work, it can provide insights into combustion quality and flame instabilities. Kurtosis values represented in Fig. 15 show relevant features concerning stability and intensity of the combustion process. The results obtained for the two conditions considered are listed in Table 5.

The trend reveals that as mixture is getting leaner, combustion dynamics in pressure as well as in structure response is changing notably. In the case of the piezo-MEMS signal, the kurtosis increases from 3.0587 at $\phi = 0.36$ to 3.3420 at $\phi = 0.18$, showing that under leaner conditions, the distribution becomes more peaked with thinner tails. It would, therefore, seem that while the general intensity of the mechanical oscillations may be lower, the system experiences more frequent, localized fluctuations around the mean with fewer extreme deviations. This may be related to intermittent local quenching or unsteady flame anchoring, common near the LBO limit. For the pressure signal, the kurtosis increases slightly from 3.0146 at $\phi = 0.36$ to 3.0651 at $\phi = 0.18$. While this is much weaker, it reflects that the probability distribution function of the pressure becomes a little more peaked, reflecting a decrease in the occurrence of large-scale pressure fluctuations. However, the latter does not necessarily point towards greater stability. Though the combustion intensity is weakened at conditions near LBO, pressure fluctuations may become more intermittent and feature localized extinction and re-ignition events that are hard to be reflected in a simple statistical

Table 5
Kurtosis values for the two test cases and both sensors.

Φ	Kurtosis	
	Accelerometer	Pressure sensor
0.36	3.0587	3.0146
0.18	3.3420	3.0651

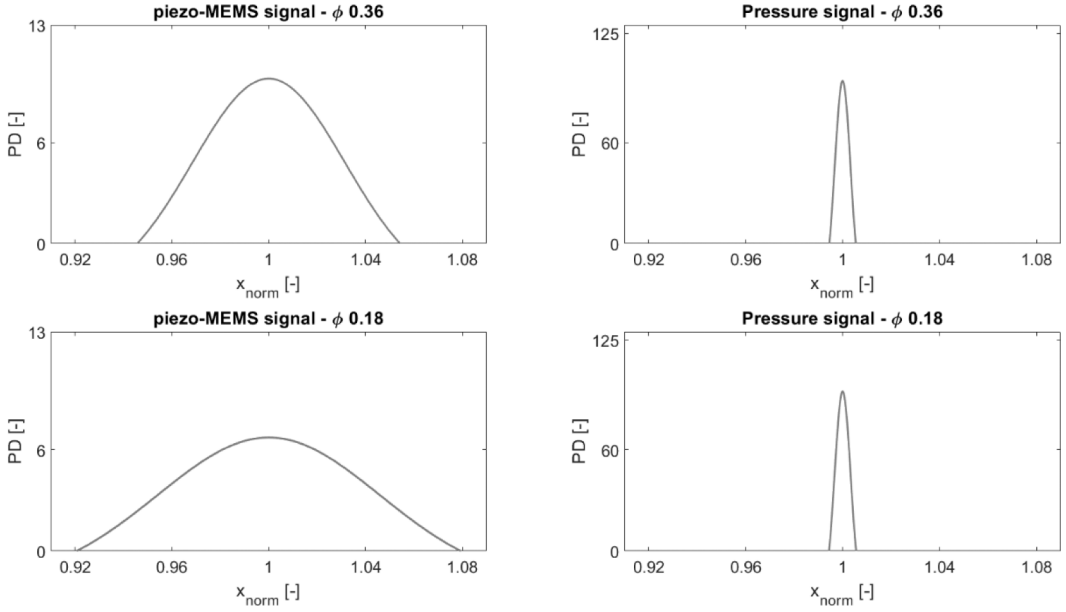

Fig. 16b. Trend of the variance normalized to 1 on a probability density scale for the time signals of the commercial pressure sensor and the microfabricated piezo-MEMS accelerometer for the two analyzed test cases.

measure. The increase in kurtosis at $\phi = 0.18$ for both signals aligns with the expected behavior of a combustion system approaching lean blowout: the overall amplitude of fluctuations decreases due to weaker combustion, but the system may experience sudden and localized deviations as the flame struggles to stabilize. This could result in sporadic high-intensity events, even if the overall signal remains less intense compared to richer mixtures. In summary, while a higher kurtosis may be indicative of a lower variance with more concentrated fluctuations at $\phi = 0.18$, it really represents the greater intermittency and unsteadiness of the combustion process as LBO is approached. It becomes less intense on average with a reduction in stability and an increase in sensitivity to external perturbations that may trigger localized extinction events. These results further highlight the fact that kurtosis can be used as an important feature not only from the point of view of distribution shape but also with respect to indicating combustion stability and lean blowout [54].

4. Conclusions

This work describes the design, fabrication, and experimental validation of a piezoelectric MEMS accelerometer for combustion instability monitoring. The device was characterized in laboratory in terms of frequency response, linearity, and noise. The experimental characterization showed that the resonance frequency of the accelerometer is 3.8 kHz, very close to the simulated results; voltage sensitivity is 0.25 mV/g, in accordance with simulation output, and total noise density equal to 41 $\mu g/\sqrt{Hz}$ at 500 Hz, comparable to many commercial accelerometers currently used for gas turbine monitoring, further establishing the suitability of the device in practical applications. To assess performance under realistic combustion conditions, the accelerometer was then tested in a high-performance 300-kW swirled combustor equipped with a reference pressure sensor. Two equivalence ratios, $\phi = 0.36$ and $\phi = 0.18$, were investigated to capture the transition from a moderately unstable regime to near-lean blowout. Statistical analysis of the sensor signals provided important information on combustion dynamics, confirming that at $\phi = 0.36$ the system is largely unstable, while at $\phi = 0.18$ the combustion regime is more unpredictable. Good correlation (DCC $>$ 0.996) between the pressure and acceleration signals during the experiment validated that combustion-induced vibrations are effectively captured by the MEMS accelerometer. The developed piezoelectric MEMS accelerometer is resulted a viable alternative to the traditional pressure sensor in combustion instability monitoring. Showing a compact design, high sensitivity, and solid performance in realistic conditions, it may become one of the most promising candidates for advanced diagnostics in gas turbines, industrial combustors, and propulsion systems. The MEMS accelerometer employed in this study features a wide operational bandwidth ranging from 0 to 5000 Hz, enabling the detection of a broad spectrum of combustion-related dynamic phenomena. It is particularly well-suited for capturing thermoacoustic instabilities, due to interactions between heat release and acoustic modes of the combustion chamber, which typically occur in the 50 Hz to 2000 Hz range, depending on the combustor geometry, acoustic boundary conditions, and operational parameters. The sensor also reliably detects Bénard–von Kármán (BvK) vortex shedding [55,56], whose characteristic frequencies generally span from a few tens of Hz up to approximately 1500 Hz, especially in bluff-body and wake-dominated flows.

Additionally, the accelerometer is capable of capturing Kelvin–Helmholtz (KH) instabilities, which originate from shear layer interactions and manifest across a broad frequency range, extending from a few tens of Hz up to several kilohertz (typically 100 Hz to 5 kHz), depending on flow velocity, shear layer thickness, and combustor configuration [55,57].

Moreover, the sensor is sensitive to combustion noise and lean blowout (LBO) precursors, which predominantly exhibit low-frequency oscillations. These are generally observed below 150 Hz, although broadband spectral content may extend into the 200–500 Hz range [51,58], particularly in proximity to blowout conditions or during thermoacoustic–hydrodynamic coupling.

Thanks to this wide frequency coverage, the sensor proves to be a promising tool not only for detecting precursors to blowout—an aspect central to this study—but also for identifying early signs of thermoacoustic instabilities in real-world combustor applications.

The sensor integration in real-time control strategies will be concentrated in future work, supported by further refinement of its applicability in combustion monitoring by extending the response to a wider equivalence ratio and flow conditions. Moreover, the long-term stability of the piezoelectric film in harsh environment (as the combustion one) will be faced, too, and new strategies to improve this property by keeping unaltered the piezoelectric behavior (i.e. doping with transition metals) will be investigated.

CRediT authorship contribution statement

M.A. Signore: Writing – original draft, Validation, Supervision, Methodology, Investigation, Formal analysis, Data curation, Conceptualization. **C. De Pascali:** Writing – original draft, Validation, Software, Data curation. **F. Quaranta:** Writing – original draft, Validation, Funding acquisition. **L. Velardi:** Writing – original draft, Validation, Methodology, Investigation, Data curation. **D. Valerini:** Writing – original draft, Validation, Investigation, Data curation. **I. Farella:** Supervision, Funding acquisition, Conceptualization. **P. Di Gloria:** Writing – original draft, Validation, Methodology, Investigation, Data curation. **M.G. De Giorgi:** Writing – original draft, Validation, Supervision, Investigation, Data curation, Conceptualization. **A. Ficarella:** Supervision, Funding acquisition, Conceptualization. **L. Francioso:** Writing – original draft, Validation, Supervision, Investigation, Funding acquisition, Data curation, Conceptualization.

Funding

The work was supported and funded by the PON R&I 2014–2020 Asse I "Investimenti in Capitale Umano" Azione IV.5 "Dottorati Innovativi sulle tematiche Green" – Corso di Dottorato in "Ingegneria dei Sistemi Complessi" XXXVII ciclo – Università del Salento" and by the PON project SMEA "*Diagnostic and prognostic methods and* Sensors *development for the health Monitoring in aEronautic and transport Applications"* (PON03PE_00067_5).

Declaration of competing interest

The authors declare that they have no known competing financial interests or personal relationships that could have appeared to influence the work reported in this paper.

Acknowledgement

The authors are very grateful to E. Melissano, A. Campa, M.C. Martucci, and P. Cretì for their preciuos support during the device fabrication.

Data availability

Data will be made available on request.

References

[1] T. Lv, V.O. Pelenovich, C. Xu, X. Zeng, D. Hou, Z. Xiong, B. Yang, F. Dong, S. Liu, Fabrication and characterization of high-temperature AlN thick-film piezoelectric accelerometer, Ceram. Int. 50 (2024) 47008–47016, https://doi.org/10.1016/j.ceramint.2024.09.051.

[2] H.E. Ahmed, S. Sahandabadi, M.J. Bhawya, M.J. Ahamed, Application of MEMS Accelerometers in Dynamic Vibration monitoring of a Vehicle, Micromachines 14 (2023) 923, https://doi.org/10.3390/mi14050923.

[3] R. Mukhiya, M. Santosh, A. Sharma, S. Santosh Kumar, S.C. Bose, R. Gopal, B. D. Pant, Fabrication and characterization of a bulk micromachined polysilicon piezoresistive accelerometer, Mater. Today: Proceed. 40 (2022) 619–621, https://doi.org/10.1016/j.matpr.2021.05.588.

[4] Y. He, C. Si, G. Han, Y. Zhao, J. Ning, F. Yang, A Novel Fabrication Method for a Capacitive MEMS Accelerometer based on Glass-Silicon Composite Wafers, Micromachines (basel) 12 (2021) 102, https://doi.org/10.3390/mi12020102.

[5] H.Y. Choi, K.S. Park, S.J. Park, U.-C. Paek, B.H. Lee, E.S. Choi, Miniature fiber-optic high temperature sensor based on a hybrid structured Fabry–Perot interferometer, Opt. Lett. 33 (2008) 2455–2457, https://doi.org/10.1364/ol.33.002455.

[6] Y.C. Lee, C.C. Tsai, C.Y. Li, Y.C. Liou, C.S. Hong, S.Y. Chu, Fabrication and function examination of PZT-based MEMS accelerometers, Ceram. Int. 47 (2021) 24458–24465, https://doi.org/10.1016/j.ceramint.2021.05.161.

[7] H.E. Ahmed, S. Sahandabadi, B. Ahamed, M.J. Ahamed, Application of MEMS Accelerometers in Dynamic Vibration monitoring of a Vehicle, Micromachines (basel) 14 (5) (2023) 24923, https://doi.org/10.3390/mi14050923.

[8] Y. Liao, H. Yang, Q. Liao, W. Si, Y. Chu, X. Chu, L. Qin, A Review of Flexible Acceleration Sensors based on Piezoelectric Materials: Performance Characterization, Parametric Analysis, Frontier Technologies, and applications, Coatings 13 (2023) 1252, https://doi.org/10.3390/coatings13071252.

[9] C. Yang, B. Hu, L. Lu, Z. Wang, W. Liu, C. Sun, A Miniaturized Piezoelectric MEMS Accelerometer with Polygon Topological Cantilever Structure, Micromachines 13 (2022) 1608, https://doi.org/10.3390/mi13101608.

[10] B. Tian, H. Liu, N. Yang, Y. Zhao, Z. Jiang, Design of a Piezoelectric Accelerometer with High Sensitivity and Low Transverse effect, Sensors 16 (2016) 1587, https://doi.org/10.3390/s16101587.

[11] O. Deubzer, "Reduction of hazardous materials in electrical and electronic equipment," Waste electrical and Electronic Equipment (WEEE) Handbook, Elsevier, Amsterdam, The Netherlands, 2019, pp. 207–230.

[12] S.A. Gurin, E. A. Pecherskaya, K. Y. Spitsyna, A. V. Fimin, D. V. Artamonov, A. E. Shepeleva, "Thin Piezoelectric Films for Micromechanical Systems," *2020 Moscow Workshop on Electronic and Networking Technologies (MWENT)*, Moscow, Russia, 2020, pp. 1-5, doi: 10.1109/MWENT47943.2020.9067450.

[13] D. Drury, K. Yazawa, A. Mis, K. Talley, A. Zakutayev, G.L. Brennecka, Understanding Reproducibility of Sputter-Deposited Metastable Ferroelectric Wurtzite $Al_{0.6}Sc_{0.4}N$ Films using In Situ Optical Emission Spectrometry, Phys. Status Solidi RRL 15 (2021) 2100043, https://doi.org/10.1002/pssr.202100043.

[14] S. Narayan, S. Milojevic, V. Gupta, Combustion monitoring in engines using accelerometer signals, Journal of Vibroengineering 21 (2019) 1552. https://doi.org/10.21595/jve.2019.20516.

[15] Y. Liu, J. Li, Y. Yan, S. Shang, Limited driving characteristics of combustion instability in a swirling flame: an experimental study, Fuel 337 (2023) 126866, https://doi.org/10.1016/j.fuel.2022.126866.

[16] W. Liu, R. Xue, J. Jiang, H. Su, X. Wang, Large Eddy simulation and Acoustic Analysis of Combustion Instability in an Annular Combustor with Low-Swirl Flames, ACS Omega 11 (2024) 21983–21993, https://doi.org/10.1021/acsomega.3c10234.

[17] J. Hunicz, M.S. Gęca, E. Ratajczyk, A.M. Andwari, L. Yang, M. Mikulski, An analytical approach to converting vibration signal to combustion characteristics of homogeneous charge compression ignition engines, Energ. Conver. Manage. 294 (2023) 117564, https://doi.org/10.1016/j.enconman.2023.117564.

[18] Q. Talal, Z. Abubakar, M.R. Shakeel, M.S. AlSwat, E.M.A. Mokheimer, Time Series and Spectral Analysis of Thermoacoustic Oscillations for Propane-Oxyfuel Combustion in a Swirl-Stabilized, Nonpremixed Combustor, ACS Omega 8 (2023) 36053–36064, https://doi.org/10.1021/acsomega.3c04144.

[19] H. Faraji, K. Heidarbeigi, S. Samadi, Characterization of vibration and noise pollution of SI engine fueled with magnetized ethanol–gasoline blends by time–frequency methods, Noise Vibr. Worldwide 52 (11) (2021) 356–364, https://doi.org/10.1177/09574565211030704.

[20] Framework (2023). Accessed 12 February 2024, https://ec.europa.eu/clima/policies/strategies/2030_en.

[21] Z. Han, M.M. Moinul Hossain, Y. Wang, J. Li, C. Xu, Combustion stability monitoring through flame imaging and stacked sparse autoencoder based deep neural networ, Applied Energy 259 (2020) 114, https://doi.org/10.1016/j.apenergy.2019.114159.

[22] G. Silvagni, V. Ravaglioli, F. Ponti, E. Corti, D. Moro, A. Brusa, N. Cavina, J. Phys. Conf. Ser. 2385 (2022) 012064, https://doi.org/10.1088/1742-6596/2385/1/012064.

[23] Y. Zhou, C. Zhang, X. Han, Y. Lin, Monitoring combustion instabilities of stratified swirl flames by feature extractions of time-averaged flame images using deep learning method, Aerosp. Sci. Technol. 109 (2021) 106443, https://doi.org/10.1016/j.ast.2020.106443.

[24] A.M. James, A.K. Agrawal, Spatially resolved chemiluminescence imaging of multiple combustion species using a single high-speed camera, Meas. Sci. Technol. 34 (2023) 125305, https://doi.org/10.1088/1361-6501/acfa18.

[25] https://buy.endevco.com/ContentStore/mktg/Downloads/EDV-6222s.pdf.

[26] https://www.pcb.com/applications/energy/combustion-dynamics.

[27] S. Brischetto, E. Carrera, Free Vibration Analysis for Layered Shells Accounting of Variable Kinematic and Thermo-Mechanical Coupling, Shock Vib. 19 (2012) 155–173, https://doi.org/10.3233/SAV-2011-0621.

[28] V. Ferrari, A. Ghisla, D. Marioli, A. Taroni, Silicon resonant accelerometer with electronic compensation of input-output cross-talk, Sens. Act. A 123–124 (2005) 258–266, https://doi.org/10.1016/j.sna.2005.03.067.

[29] M.A. Hopcroft, W.D. Nix, T.W. Kenny, What is the Young's Modulus of Silicon? J. Microelectromech. Syst. 19 (2010) 229–238, https://doi.org/10.1109/JMEMS.2009.2039697.

[30] D. Chicot, P. Démarécaux, J. Lesage, Apparent interface toughness of substrate and coating couples from indentation tests, Thin Solid Films 283 (1996) 151–157, https://doi.org/10.1016/0040-6090(96)08763-9.

[31] M.A. Signore, G. Rescio, C. De Pascali, V. Iacovacci, P. Dario, A. Leone, F. Quaranta, A. Taurino, P. Siciliano, L. Francioso, Fabrication and characterization of AlN-based flexible piezoelectric pressure sensor integrated into an implantable artificial pancreas, Sci. Rep. 9 (2019) 17130, https://doi.org/10.1038/s41598-019-53713-1.

[32] M.A. Signore, A. Taurino, M. Catalano, M. Kim, Z. Che, F. Quaranta, P. Siciliano, Growth assessment of (002)-oriented AlN thin films on Ti bottom electrode deposited on silicon and kapton substrates, Mater. Des. 119 (2017) 151–158, https://doi.org/10.1016/j.matdes.2017.01.035.

[33] M.A. Signore, L. Velardi, C. De Pascali, I. Kuznetsova, L. Blasi, F. Biscaglia, F. Quaranta, P. Siciliano, L. Francioso, Effect of silicon-based substrates and deposition type on sputtered AlN thin films: Physical & chemical properties and suitability for piezoelectric device integration, Appl. Surf. Sci. 599 (2022) 154017, https://doi.org/10.1016/j.apsusc.2022.154017.

[34] W. Yong-Liang, C. Hong-Ling, Y. Bai-Ru, C. Xiang-Rong, First-Principle Calculations of Elastic Properties of Wurtzite-Type Aluminum Nitride under pressure, Commun. Theor. Phys. (beijing, China) 49 (2008) 489–492, https://doi.org/10.1088/0253-6102/49/2/50.

[35] E. Guler, M. Guler, High pressure Elastic Properties of Wurtzite Aluminum Nitrate, Chin. J. Phys. 52 (2014) 1625–1635, https://doi.org/10.6122/CJP.20140610A.

[36] W.J. Song, D.J. Cha, Temporal kurtosis of dynamic pressure signal as a quantitative measure of combustion instability, Appl. Therm. Eng. 104 (2016) 577–586, https://doi.org/10.1016/j.applthermaleng.2016.05.094.

[37] M. Reusch, S. Cherneva, Y. Lu, A. Zukauskait, L. Kirste, K. Holc, M. Datcheva, D. Stoychev, V. Lebedev, O. Ambacher, Microstructure and mechanical properties of stress-tailored piezoelectric AlN thin films for electro-acoustic devices, Appl. Surf. Sci. 407 (2017) 307–314, https://doi.org/10.1016/j.apsusc.2017.02.147.

[38] V. Moraes, H. Riedl, R. Rachbauer, S. Kolozsvari, M. Ikeda, L. Prochaska, S. Paschen, P.H. Mayrhofer, Thermal conductivity and mechanical properties of AlN-based thin films, J. Appl. Phys. 119 (2016) 225304, https://doi.org/10.1063/1.4953358.

[39] S.-R. Jian, G.-J. Chen, H.-G. Chen, J.-C. Jang, Y.-Y. Liao, P.-F. Yang, Y.-S. Lai, M.-R. Chen, H.-L. Kao, J.-Y. Juang, Cross-sectional transmission electron microscopy studies for deformation behaviors of AlN thin films under Berkovich nanoindentation, J. Alloy. Compd. 504S (2010) S395–S398, https://doi.org/10.1016/j.jallcom.2010.02.050.

[40] L. Kolaklieva, V. Chitanov, A. Szekeres, K. Antonova, P. Terziyska, Z. Fogarassy, P. Petrik, I.N. Mihailescu, L. Duta, Pulsed Laser Deposition of Aluminum Nitride Films: Correlation between Mechanical, Optical, and Structural Properties, Coatings 9 (2019) 195, https://doi.org/10.3390/coatings9030195.

[41] E. Osterlund, J. Kinnunen, V. Rontu, A. Torkkeli, M. Paulasto-Krockel, Mechanical properties and reliability of aluminum nitride thin films, J. Alloy. Compd. 772 (2019) 306–313, https://doi.org/10.1016/j.jallcom.2018.09.062.

[42] I. Yonenaga, T. Shima, M.H.F. Sluiter, Nano-Indentation Hardness and Elastic Moduli of Bulk Single-Crystal AlN, Jpn. J. Appl. Phys. 41 (2002) 4620–4621, https://doi.org/10.1143/JJAP.41.4620.

[43] S. S. Rao, Mechanical Vibrations (Pearson education, 2011).

[44] F. Alves, R. Rabelo, G. Karunasiri, Dual Band MEMS Directional Acoustic Sensor for Near Resonance operation, Sensors 22 (2022) 5635, https://doi.org/10.3390/s22155635.

[45] V. Kumar, S. Tiwari, G. Pillai, R. Pratap, S.A. Chandorkar, Synchronized Opto-Electro-Mechanical Measurements for Estimation of Energy Dissipation in Thin-Film-Piezoelectric-on-Substrate MEMS/NEMS Devices, J. Microelectromech. Syst. 33 (2024) 793, https://doi.org/10.1109/JMEMS.2024.3465507.

[46] F.A. Levinzon, Fundamental Noise Limit of Piezoelectric Accelerometer, IEEE Sens. J. 4 (2004) 108–111.

[47] P. Giannelli, A. Bulletti, L. Capineri, Charge-mode interfacing of piezoelectric interdigital Lamb wave transducers, Electron. Lett 52 (2016) 894–896, https://doi.org/10.1049/el.2016.0804.

[48] C.D. Martin, J.E. Shepherd, Low temperature autoignition of Jet a and surrogate jet fuel, J. Loss Prev. Process Ind. 71 (2021) 104454, https://doi.org/10.1016/j.jlp.2021.104454.

[49] NASA (1983), Preliminary Tests of a High-Temperature Advanced Combustion System, NASA Technical Memorandum 86060.

[50] T. Lieuwen, V. Yang, Combustion Instabilities in Gas Turbine Engines: Operational Experience, Fundamental Mechanisms, and Modeling, Prog. Astronaut. Aeronaut. (2005).

[51] M.G. De Giorgi, P. Di Gloria, D. Fontanarosa, A. Ficarella, Advanced multiscale modal and frequency analysis of swirling spray flame near to lean blowout, Case Studies in Thermal Engineering 60 (2024), https://doi.org/10.1016/j.csite.2024.104651. ISSN 2214-157X.

[52] T. Lieuwen, Combustion driven oscillations in gas turbines, Turbomachinery International 44 (1) (January 2003) 16–18.

[53] International Standard, ISO 3534-1:2006, Statistics — Vocabulary and symbols — Part 1: General statistical terms and terms used in probability, Edition 2, 2006.

[54] J. Liu, H. Zhang, H. Zhao, Analysis of Combustion Instability in Internal Combustion Engines using Kurtosis and Wavelet Transform, Int. J. Engine Res. 19 (2) (2018) 210–225, https://doi.org/10.1177/1468087417718440.

[55] A. Prasad, C.H.K. Williamson, The Instability of the Shear Layer Separating from a Bluff Body, Journal of Fluid Mechanics 333 (1997) 375–402, https://doi.org/10.1017/S0022112096004326.

[56] Santosh J. Shanbhogue, Sajjad Husain, Tim Lieuwen, Lean blowoff of bluff body stabilized flames: Scaling and dynamics, Progress in Energy and Combustion

Science, Volume 35, Issue 1, 2009, Pages 98-120, ISSN 0360-1285, https://doi.org/10.1016/j.pecs.2008.07.003.
[57] Marc Füri, Paul Papas, Redha M. Raïs, Peter A. Monkewitz, The effect of flame position on the Kelvin-Helmholtz instability in non-premixed jet flames, Proceedings of the Combustion Institute, Volume 29, Issue 2, 2002, Pages 1653-1661, ISSN 1540-7489, https://doi.org/10.1016/S1540-7489(02)80203-6.
[58] Meng Han, Quanhong Xu, Xiao Han, Yuzhen Lin, Dynamics of stratified swirl flame near lean blow out, Propulsion and Power Research, Volume 10, Issue 3, 2021, Pages 235-246, ISSN 2212-540X, https://doi.org/10.1016/j.jppr.2021.07.002.